Alloying-induced enhancement of thermopower in the Dirac-semimetal system $Cd_{3-x}Zn_xAs_2$

J. Fujioka,[1,*] M. Kriener,[2,†] D. Hashizume,[2] Y. Yamasaki,[3] Y. Taguchi,[2] and Y. Tokura[2,4,5]

[1]*Division of Materials Science, University of Tsukuba, 1-1-1 Tennodai, Tsukuba, Ibaraki 305-8573, Japan*

[2]*RIKEN Center for Emergent Matter Science (CEMS), Wako 351-0198, Japan*

[3]*National Institute of Material Science, Tsukuba, Ibaraki 305-0047, Japan*

[4]*Department of Applied Physics and Quantum-Phase Electronics Center (QPEC), University of Tokyo, Tokyo 113-8656, Japan*

[5]*Tokyo College, University of Tokyo, Hongo, Tokyo 113-8656, Japan*

(Received 11 March 2021; revised 13 July 2021; accepted 25 August 2021; published 7 September 2021)

Cd_3As_2 is one of the prototypical topological Dirac semimetals. Here, we manipulate the band inversion responsible for the emergence of Dirac nodes by alloying Cd_3As_2 with topologically trivial Zn_3As_2. The carrier density monotonically decreases and the resistivity is enhanced as x is increased. For larger x, the thermoelectric figure of merit exhibits comparably large values exceeding 0.3 at room temperature, due to the combined effects of a strong enhancement of the thermopower, an only moderate increase in the resistivity, and a suppression of the thermal conductivity. Complementary quantum-oscillation data and optical-conductivity measurements allow us to infer that the Dirac nodes are gapped out, and a band structure with a partly flat dispersion likely emerges in the higher-x region in $Cd_{3-x}Zn_xAs_2$.

DOI: 10.1103/PhysRevMaterials.5.094201

I. INTRODUCTION

Quantum transport of relativistic electrons in topological semimetals has been an issue of great interest in topological materials science [1]. In such materials, the quantum state of the Dirac or Weyl electrons is strongly coupled to the crystal symmetry, and hence the engineering of the electronic symmetry is a promising way to search for exotic quantum transport of such quasiparticles. In recent years, more and more materials have been theoretically predicted [2] and experimentally found to be a topological semimetal. Prototypical materials include A_3Bi with A = Na, K, Rb [3–5] and Cd_3As_2 [6–13].

Among them, Cd_3As_2 possesses a simple band structure with an electron charge carrier density of $\sim 10^{18}$ cm^{-3}. It has long been known for its large mobility of $\sim 10^4$ cm^2 V^{-1} s^{-1} at room temperature [14]. Recently, an even higher value of almost $\sim 10^7$ cm^2 V^{-1} s^{-1} was reported at low temperatures due to a linear band dispersion and strongly suppressed backscattering events of the charge carriers [8]. The nontrivial topology of this system, namely, an inversion of conduction and valence bands which are of different character, manifests in two Dirac nodes in the proximity of the Fermi energy E_F [6], which are protected by both time-reversal symmetry and rotational symmetry of the crystal lattice [6]. For example, it has been demonstrated that the breakdown of time-reversal symmetry via the application of a magnetic field creates a Weyl semimetallic state with negative magnetoresistance due to the chiral anomaly [15–18], a hallmark of the underlying nontrivial physics.

Another way to control the electronic structure in such systems is to manipulate the band inversion directly. It has been proposed that the chemical substitution of Cd with Zn changes the sign of the band gap from negative (band inversion) to positive, resulting in the topological transition from a Dirac semimetal to a trivial insulator [19–22]. Indeed, in contrast to Cd_3As_2, Zn_3As_2 is a topologically trivial semiconductor with a hole carrier density of $\sim 10^{17}$ cm^{-3} and a much lower room-temperature mobility of only ~ 10 cm^2 V^{-1} s^{-1} [14]. Hence a depletion of the charge carriers and a topological phase transition from the Dirac semimetal Cd_3As_2 to trivial Zn_3As_2 are expected when alloying these two systems. Indeed, Lu *et al.* found experimental indications of this transition in $Cd_{3-x}Zn_xAs_2$ in magnetotransport measurements [22] at $x \sim 1.1$ on the basis of an enhanced resistivity upon cooling as well as a thorough analysis of Shubnikov–de Haas (SdH) oscillations. Recent studies on thin films of $Cd_{3-x}Zn_xAs_2$ also support this scenario qualitatively [23–25], although the topological phase transition takes place already at $x \sim 0.6$ [25]. We note that a similar transition is proposed to occur in the related $Cd_3As_{2-y}P_y$ on the basis of angle-resolved photoemission spectroscopy data [26].

Given the remarkably high mobility of the electron charge carriers, Cd_3As_2 is expected to bear the potential for a good thermoelectric performance with possibly large power factors S_{xx}^2/ρ_{xx}, S_{xx} and ρ_{xx} being the longitudinal thermopower and resistivity, respectively [27]. Indeed, a recent study reported $S_{xx}^2/\rho_{xx} \sim 1.6 \times 10^{-3}$ W K^{-2} m^{-1} along with a fairly small thermal conductivity $\kappa_{xx} \sim 5$ W K^{-1} m^{-1}, yielding $ZT \sim 0.1$ at room temperature [28]; ZT represents the figure of merit $ZT = S_{xx}^2 T/(\rho_{xx}\kappa_{xx})$ as a measure of the thermoelectric efficiency. This value further increases in the presence of a magnetic field B, exceeding unity at $B = 7$ T and $T = 375$ K [29] mainly due to field-induced suppression of κ_{xx}. Since these parameters also depend on the actual charge carrier density [30], it is promising to study the thermoelectric performance upon alloying. However, there are only a few studies

*Corresponding author: fujioka@ims.tsukuba.ac.jp

†Corresponding author: markus.kriener@riken.jp

which comprehensively address the alloying-induced evolution of the charge or thermal transport properties and the electronic states in $Cd_{3-x}Zn_xAs_2$.

In this paper, we have measured transport, thermoelectric properties, and the charge dynamics upon Zn alloying in $Cd_{3-x}Zn_xAs_2$ with $0 \leqslant x \leqslant 1.2$. With increasing x, the carrier density is monotonically reduced and the Seebeck coefficient is largely enhanced, exceeding 300 μV/K at 300 K for $x = 1.2$. At low temperatures, we could confirm the reported metal-insulator transition with Zn alloying [22]. At the same time, Zn alloying suppresses the thermal conductivity while the resistivity above the metal-insulator transition temperature is enhanced only modestly due to the alloying-induced disorder. Hence the thermoelectric figure of merit is greatly enhanced, exceeding 0.3 at room temperature, i.e., more than three times the value reported for pure Cd_3As_2. Complementary analyses of quantum-oscillation and optical-conductivity data suggest an x-dependent change in the band structure dispersion in the higher-x region which promotes the enhancement of the figure of merit.

This paper is organized as follows: First, we will present electric and thermal transport data with enhanced ZT values. Then we will analyze magnetotransport and optical-spectroscopy data which point toward the scenario of an x-dependent change in the band structure at E_F giving rise to the observed large room-temperature ZT values. We will finish with a discussion of our findings and conclude with a summary of the paper.

II. EXPERIMENTAL METHODS

Single-crystalline samples of Cd_3As_2 were grown by the Bridgman technique, while polycrystalline samples of $Cd_{3-x}Zn_xAs_2$ were synthesized by conventional melt growth. In both cases, stoichiometric ratios of the constituent elements were mixed inside a glovebox, transferred into quartz tubes, and eventually sealed while evacuated. In the Bridgman-method growth, the temperature of the upper (lower) heater was set to 900 °C (600 °C). The evacuated quartz tubes were kept for 12 h at 900 °C and then lowered with a speed of 2 mm/h. After the quartz tubes had reached the lower heater, they were slowly cooled down to room temperature. Melt-grown batches were kept for 48 h at 800–950 °C depending on the composition and slowly cooled down to room temperature afterwards. We have analyzed the composition of Cd, Zn, and As by energy-dispersive x-ray spectroscopy analysis (EDX) using a scanning electron microscopy imaging system (see Fig. S1 in the Supplemental Material [31]).

Resistivity and the Hall effect were measured by a conventional five-probe method in a commercial system [physical property measurement system (PPMS), Quantum Design]. The thermopower and thermal conductivity were measured in a home-built setup inserted into a PPMS while applying a temperature gradient by using a chip heater attached on one side of the sample. The temperature gradient is monitored by employing commercial thermocouples. We confirmed the linear relation between the temperature difference measured by the thermocouples and the input power generated at the chip heater in the measured temperature region (see Fig. S2 in the Supplemental Material). The heater power was set so

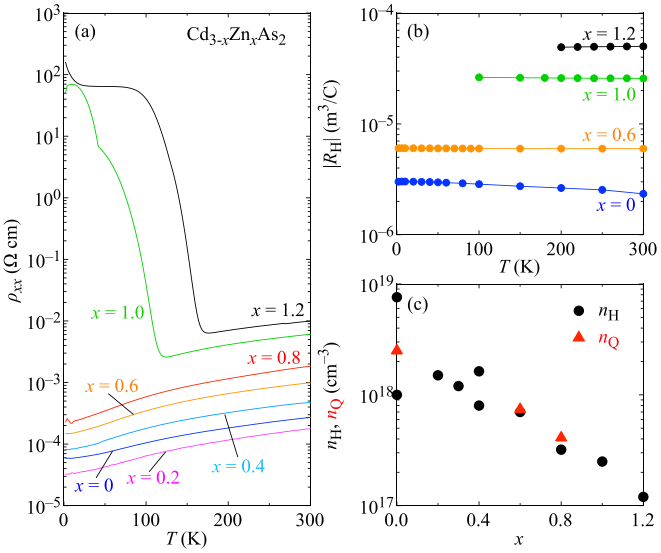

FIG. 1. Temperature dependence of (a) resistivity and (b) absolute value of the Hall coefficient $|R_H|$ for $Cd_{3-x}Zn_xAs_2$. Here, R_H is negative for all x and the whole temperature range examined. (c) Carrier densities as a function of doping level x. Here, n_H (n_Q) denotes the carrier density derived from Hall coefficient data (quantum oscillations). n_Q is derived assuming an isotropic Fermi surface (of spherical shape).

that the typical temperature difference between the thermocouples became about 1 K. While all quantities used for determining the thermoelectric figure of merit, i.e., resistivity, thermopower, and thermal conductivity, were measured on polycrystalline samples, the optical spectroscopy on the undoped compound was measured on a single-crystalline sample. The reflectivity spectra at nearly normal incidence were measured between room temperature and 10 K in the energy region of 0.008–5 eV. In the case of single-crystalline Cd_3As_2, a sample surface with $[11\bar{2}]$ orientation was polished. Then the spectra were measured with $[1\bar{1}0]$ light polarization. As for $Cd_{3-x}Zn_xAs_2$, reflectivity spectra were measured with unpolarized light. A Fourier transform spectrometer and a grating-type monochromator equipped with a microscope were employed in the photon energy range 0.008–0.7 eV and 0.5–5 eV, respectively. Measurements in the energy range of 3–40 eV were carried out at room temperature by using synchrotron radiation at UV-SOR, Institute for Molecular Science (Okazaki). For Kramers-Kronig transformations, we adopted suitable extrapolation procedures for energy ranges which were not accessible by the used experimental setups: Below 0.008 eV the Hagen-Rubens-type (metal) or constant-reflectivity (insulator) extrapolation was used, respectively. Above 40 eV an ω^{-4}-type extrapolation was utilized.

III. RESULTS

Figure 1(a) shows the temperature dependence of the longitudinal resistivity ρ_{xx} for $Cd_{3-x}Zn_xAs_2$. In the low-x region ($0 \leqslant x \leqslant 0.6$), the resistivity decreases upon lowering temperature; that is, the system behaves like a metal. The residual resistivity at 5 K is enhanced with increasing x as compared with our pure Cd_3As_2 sample except for $x = 0.2$. An upturn

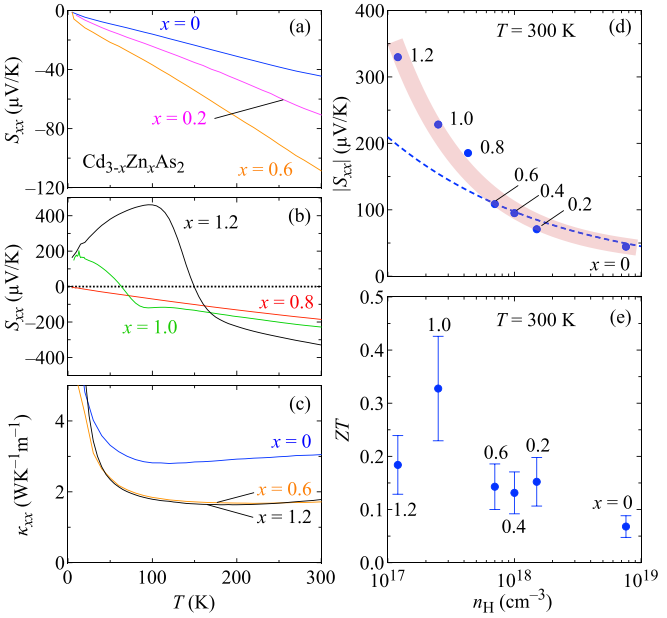

FIG. 2. Temperature dependence of the Seebeck coefficient (a) for $x = 0$, 0.2, and 0.6 and (b) for $x = 0.8$, 1.0, and 1.2. (c) Thermal conductivity for $x = 0$, 0.6, and 1.2. (d) Absolute value of the Seebeck coefficient $|S_{xx}|$ and (e) figure of merit ZT at 300 K plotted as a function of the charge carrier density n_H for $0 \leqslant x \leqslant 1.2$. In (d), the dashed curve indicates the semiclassical expectation $|S_{xx}| \propto n^{-1/3}$ assuming a k-linear band dispersion. The broad light-red shaded curve is merely a guide to the eye. In (e), the vertical bar at each data point reflects the scattering of the results obtained on different samples with the same composition.

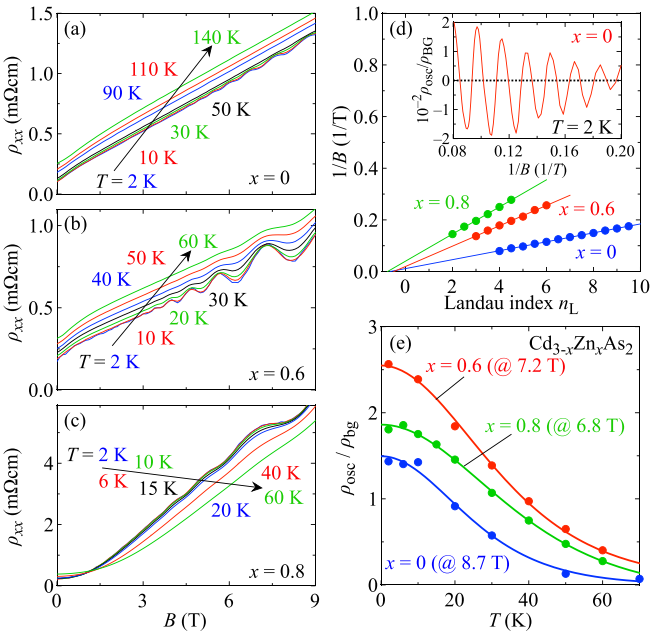

FIG. 3. Magnetoresistivity at various temperatures for (a) $x = 0$, (b) 0.6, and (c) 0.8, respectively. (d) Landau level fan diagram for $x = 0$ (blue), 0.6 (red), and 0.8 (green) at $T = 2$ K. In the inset, background-corrected quantum oscillations ρ_{osc}/ρ_{BG} for $x = 0$ are shown as a function of $1/B$. (e) Temperature dependence of the amplitude of ρ_{osc}/ρ_{BG} at selected field strengths as indicated in brackets next to the respective Zn concentrations [color code is the same as in (d)].

is clearly observed at ∼120 and ∼170 K for $x = 1.0$ and $x = 1.2$, respectively, highlighting the metal-to-insulator transition in these larger-x samples. The overall qualitative temperature dependence of the resistivities of $x = 1.0$ and 1.2 is similar. However, at very low temperatures there is a downturn in ρ_{xx} of the sample with $x = 1.0$, while the resistivity of the sample with $x = 1.2$ increases again after exhibiting a broad plateau between ∼30 and ∼80 K. Specifically, the resistivity shows a small thermal hysteresis near the onset temperature of the metal-insulator transition. These features are clearly distinct from what is expected for a conventional insulator, the resistivity of which monotonically increases upon decreasing temperature.

Figure 1(b) summarizes the temperature dependence of the absolute value of the Hall coefficient R_H (see also Fig. S4). For all x, R_H is nearly temperature independent, and its sign is negative, indicating that the conduction in all examined samples is of electron type. Estimated carrier densities n_H at room temperature assuming a single carrier model are plotted against respective Zn concentrations in Fig. 1(c), together with n_Q estimated from quantum-oscillation data (see Fig. 3). As expected the absolute value of the carrier density monotonically decreases as a function of x from the order of $\sim 3 \times 10^{18}$ cm^{-3} for $x = 0$ down to 1.2×10^{17} cm^{-3} for $x = 1.2$, reflecting the depletion of the electron-type carriers when going from n-type Cd_3As_2 to p-type Zn_3As_2. However, the charge neutrality point, i.e., the Cd:Zn ratio where the sign change of R_H takes place, is not reached up to $x = 1.2$. We observe this crossover in slightly-larger-x samples around $x \sim 1.5$ (not shown). The metallic samples $x \leqslant 0.8$ investigated here exhibit mobilities of $\sim 10^5$ cm^2 V^{-1} s^{-1} at 2 K and $\sim 10^4$ cm^2 V^{-1} s^{-1} at 300 K, respectively. We note that several properties, such as residual resistivity, charge carrier density, etc., of this material are rather sample dependent as shown in Fig. 1(c); For $x = 0$ and 0.4, two charge carrier densities measured on two different samples are shown, respectively. Such and even larger variations have been also reported for the parent material Cd_3As_2; see, e.g., Ref. [8]. This is possibly related to differences in the (Cd,Zn):As ratio. In Cd_3As_2, ideally one-fourth of the Cd lattice sites are unoccupied, and these vacancies seem to order in a chiral way along the c axis which may differ from sample to sample even if these samples were cut from the same initial batch [32]; cf. also the discussions in Refs. [7,8].

Thermoelectric and thermal-transport data are summarized in Fig. 2. The temperature dependence of the Seebeck coefficient S_{xx} is shown in Figs. 2(a) and 2(b) for $x \leqslant 0.6$ and $x \geqslant 0.8$, respectively. In the region $x \leqslant 0.8$, S_{xx} is negative and nearly proportional to temperature, which is often observed in conventional metals and semiconductors. By contrast, S_{xx} exhibits a nonmonotonic temperature dependence for larger x: Below approximately 100 and 170 K, S_{xx} deviates significantly from a temperature-linear behavior for $x = 1.0$ and 1.2, respectively. In particular, S_{xx} exhibits a sign change and becomes positive upon further cooling. Moreover, these temperatures nearly coincide with the upturn observed in resistivity data [see Fig. 1(a)].

The longitudinal thermal conductivity κ_{xx} is shown for selected x in Fig. 2(c). For all samples, κ_{xx} is almost temperature independent down to ∼100 K but steeply increases towards lower temperatures possibly due to an enhancement of the phonon mean-free path. Interestingly, in the thermal conductivity there are no characteristic anomalies visible between 50 and 200 K in clear contrast to resistivity (steep upturn) and thermopower data (clear slope change) even for $x = 1.2$, where these are most pronounced.

Absolute values of the Seebeck coefficient $|S_{xx}|$ at 300 K are replotted as a function of charge carrier density $n_{\rm H}$ in Fig. 2(d). The respective Zn concentrations x are given for each data point. Apparently, $|S_{xx}|$ increases monotonically with decreasing $n_{\rm H}$: For our pure Cd_3As_2 sample, we find $|S_{xx}| = 44\ \mu$V/K. For $x = 1.2$, $|S_{xx}|$ is enhanced by more than a factor of 6, exceeding 300 μV/K. This behavior is qualitatively consistent with the case of typical semiconductors or metals, where, according to Mott's formula, $|S_{xx}|$ is inversely proportional to $E_{\rm F}$, which decreases here as indicated by the depletion of the electron carrier density with x; cf. Fig. 1(c). The dashed curve in Fig. 2(d) indicates the expected charge-carrier-density dependence of $|S_{xx}|$ ($\propto n^{-1/3}$) in the semiclassical framework of Mott's formula with the assumption of a k-linear band dispersion. Apparently, this curve fits well to the experimental data for $x \leqslant 0.6$ but clearly falls short for larger x.

The presented quantities allow us to calculate the thermoelectric figure of merit $ZT = S_{xx}^2 T/(\rho_{xx}\kappa_{xx})$, the room-temperature values of which are plotted against $n_{\rm H}$ in Fig. 2(e). As compared with pristine Cd_3As_2 ($ZT = 0.07$), ZT increases with x and exhibits a maximum $ZT = 0.33$ for $x = 1.0$, a fairly large room-temperature value of the figure of merit. Here, we append error bars of 30% on the basis of the typical variability of results because the values of ρ_{xx}, S_{xx}, and κ_{xx} are not precisely reproducible and depend on the sample used for the measurement, as already discussed above.

To obtain further insight into what mechanism might be responsible for the observed enhancement of the thermoelectric efficiency as represented by ZT, we investigated the impact of Zn alloying on the electronic structure in $Cd_{3-x}Zn_xAs_2$ by analyzing magnetoresistivity. Experimental data along with analyses of SdH oscillations are summarized in Fig. 3. The magnetoresistivity for $x = 0$, 0.6, and 0.8 is shown in Figs. 3(a), 3(b), and 3(c), respectively. For $x = 0$ and 0.6, the resistivity is nearly proportional to the magnetic field and exhibits quantum oscillations, i.e., SdH [31]. Such a B-linear magnetoresistivity is often observed in Dirac semimetals and is one characteristic feature of the highly mobile Dirac electrons [1]. Similar SdH oscillations are also observed for $x = 0.8$ while the magnetoresistivity is rather quadratic in B in the low-field region.

Figure 3(d) contains the corresponding Landau level (LL) fan diagrams with the oscillation frequency $1/B$ plotted against the Landau index $n_{\rm L}$. It is known that the slope of the index plot corresponds to the extremal cross-sectional area of the Fermi surface B_F and the intercept indicates the phase ϕ [33]. These were extracted according to the Lifshitz-Onsager quantization rule $B_F/B = n_{\rm L} - \phi$ from the data shown in Figs. 3(a)–3(c) after subtracting the background magnetoresistivity $\rho_{\rm BG}$ by approximating it with a polynomial. The resulting oscillation part $\rho_{\rm osc}/\rho_{\rm BG}$ is shown for $x = 0$ in the inset to Fig. 3(d). Then we assigned integer and half-integer indices to the peak and valley positions in the magnetoresistivity data, respectively, as described in more detail, e.g., in Ref. [34]. The linearity of the fan plot up to the quantum limit may be a consequence of small Zeeman splitting in this system. From the slope of the LL fan diagrams, the oscillation frequency B_F is estimated to be 58, 25, and 18 T for $x = 0$, 0.6, and 0.8, respectively.

Figure 3(e) shows the temperature dependence of the background-corrected quantum oscillations $\rho_{\rm osc}/\rho_{\rm BG}$ at selected magnetic fields. From the thermal damping of the oscillation amplitudes upon warming, the cyclotron mass is estimated to be $0.051m_0$, $0.033m_0$, and $0.029m_0$ in units of the bare electron mass m_0 for $x = 0$, 0.6, and 0.8, respectively, by employing the Lifshitz-Kosevich formula [34]. We note that the Fermi velocity is nearly independent of the carrier density, suggesting that the band dispersion is close to k linear in this range of x. Table I summarizes these and additional parameters extracted from the SdH oscillations.

To obtain further insight into the electronic state, Fig. 4(a) shows the optical-conductivity spectra at 10 K for $x = 0$, 0.8, and 1.2. Spiky structures below 0.1 eV are ascribed to phonon excitations. A clear Drude peak is observed below 0.05 eV for $x = 0$ but is missing for $x = 0.8$ and 1.2. Since the carrier density is much lower for $x = 0.8$ than for $x = 0$, the Drude response likely lies below the lower limit of the measurable energy range, whereas the resistivity shows a metallic behavior even at low temperature. As a common feature in all three samples, the interband electron excitation from the valence band to the conduction band manifests itself as a very slow increase in the optical conductivity as a function of the phonon energy, which is often observed in gapless or small-gap semimetals or semiconductors [35–40]. Moreover, for each sample a small peak or kink is observed at about 0.2, 0.3, and 0.4 eV for $x = 0$, 0.8, and 1.2, respectively, as indicated with black triangles in Fig. 4(a). We note that similar features are identified in the data taken at different temperatures, assuring us that these kinks are an intrinsic feature. According to previous studies, the kink is assigned to the threshold of the interband transition of the Dirac band. In particular, the energy of the kink roughly corresponds to twice the Fermi level measured from the Dirac node, given the electron-hole symmetric band structure [36–38]. In the scheme of a rigid band model, the energy of the kink is expected to be reduced with increasing x, or equivalently with decreasing carrier density. On the contrary, the result shows that the energy of the kink is enhanced as x increases. This suggests that the rigid band model is no longer valid in the heavily alloyed region and a gap has likely opened in the case of the larger Zn concentration $x = 1.2$ as schematically illustrated in Fig. 4(c), in comparison with $x = 0$ shown in Fig. 4(b).

IV. DISCUSSION

Finally, we will discuss the relevance of the observed electronic structure to the observed enhancement of the figure of merit exceeding 0.3 at room temperature. In the present case of a Dirac dispersion, the Fermi energy should be scaled to the Fermi wave number $k_{\rm F}$, which is proportional to $n^{1/3}$. Ac-

TABLE I. Results of the analyses of the Shubnikov–de Haas (SdH) oscillations in magnetoresistivity data. Here, k_F denotes the Fermi wave vector, n_Q denotes the electron-type charge carrier density as estimated from SdH oscillations, m_c/m_0 gives the cyclotron mass in units of the electron mass m_0, v_F is the Fermi velocity, T_D refers to the Dingle temperature, and τ_Q refers to the respective scattering time.

x	k_F (Å^{-1})	n_Q (cm^{-3})	m_c/m_0	v_F (m/s)	T_D (K)	τ_Q (s)
0	0.042	2.5×10^{18}	0.051	9.4×10^5	12	1.0×10^{-13}
0.6	0.028	7.4×10^{17}	0.033	9.9×10^5	26	4.7×10^{-14}
0.8	0.023	4.1×10^{17}	0.029	9.3×10^5	10	1.2×10^{-13}

cording to Mott's formula, $|S_{xx}|$ is inversely proportional to E_F and thus is expected to scale with $n^{-1/3}$. As shown in Fig. 2(d) (dashed curve), the charge-carrier-density dependence of $|S_{xx}|$ is consistent with this semiclassical scaling for higher carrier densities, i.e., above 6×10^{17} cm^{-3}, which corresponds to $x \lesssim 0.6$. However, when further increasing the Zn concentration, the coincidence becomes worse and eventually deviates significantly when the electron carriers become very diluted. In general, quantum oscillations are a highly sensitive probe of the electronic states in the vicinity of E_F while the Seebeck coefficient is strongly influenced or determined by the electronic states in an energy range of $\pm 4k_BT$ around E_F [41]. Hence, in the present case, the Seebeck coefficient may probe the energy dispersion in the energy range of $E_F/k_B \pm 1200$ K. Thus the significant discrepancy between the experimental Seebeck coefficients and the expectation in the semiclassical model is likely to indicate that the band dispersion away from E_F is not linear in k any more in the heavily Zn-alloyed samples with $x > 0.6$ as sketched in Fig. 4(c). This strongly supports our initial working hypothesis that the Zn alloying is a tool to tailor and finely tune the band structure in the Dirac semimetal Cd_3As_2 .

The remaining question to be addressed is the origin of the thermally induced metal-insulator transition as indicated by the pronounced enhancement of ρ_{xx} below ~200 K for $x \geqslant 0.8$, which is also reflected in the nonmonotonous temperature dependence of the thermopower. Older literature reported an alloying-induced structural transition in $Cd_{3-x}Zn_xAs_2$ [20]. In order to look for a possible link between these two features, we performed temperature-dependent powder x-ray diffraction experiments on a sample with $x = 1.2$ but could not find any hint of a structural change upon cooling [31]. Hence the origin of this remarkable temperature-dependent change in resistivity and thermopower remains an unclear and interesting phenomenon to be elucidated in future studies.

V. SUMMARY

In summary, we investigated the charge and thermal transport, thermopower, and optical properties of $Cd_{3-x}Zn_xAs_2$, focusing on engineering the band structure by alloying the Dirac semimetallic Cd_3As_2 with topologically trivial Zn_3As_2. Associated with this alloying, the bands at the Fermi level are likely flattened, resulting in a strong enhancement of the thermopower. Moreover, the thermal conductivity is suppressed while the resistivity remains reasonably small, yielding a fairly large figure of merit $ZT = 0.33$ at $T = 300$ K. Our findings demonstrate that alloying is a tool to control the band structure in Dirac semimetals and that such systems can be very promising starting points to look for an enhanced thermoelectric performance.

ACKNOWLEDGMENTS

We thank D. Maryenko, T. Koretsune, R. Arita, T. Ideue, T. Liang, and A. Kikkawa for useful discussions and technical support. This work was partly supported by Grants-in-Aid for Scientific Research (No. 24224009, No. 15K05140, No. 16H00981, No. 18H01171, No. 18H04214, and No. 16H06345) from MEXT and by PRESTO (No. JPMJPR15R5) and CREST (No. JPMJCR16F1), JST (No. JP16H00924), Japan.

J.F. and M.K. contributed equally to this work.

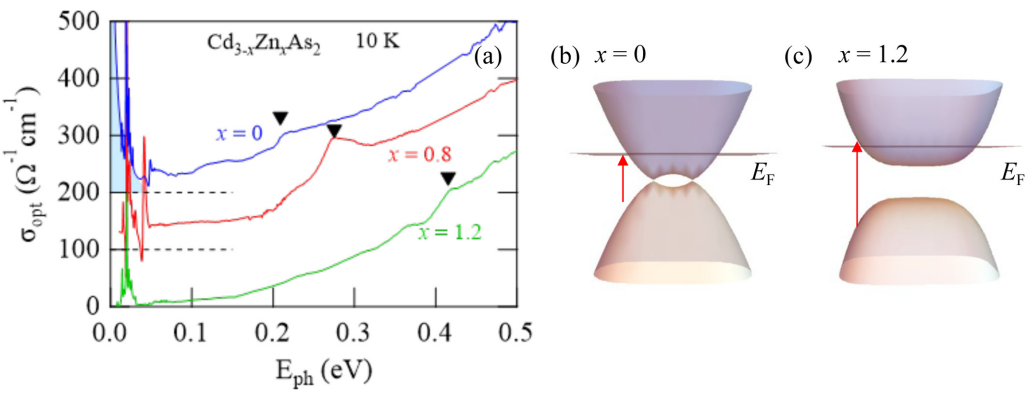

FIG. 4. (a) Optical-conductivity spectra at 10 K for $x = 0$ (blue), 0.8 (red), and 1.2 (green). The spectra are shifted by 100 Ω^{-1} cm^{-1} with respect to each other for clarity. Solid black lines indicate the respective offsets. Triangles denote the threshold of interband transitions. The shaded region for $x = 0$ denotes the Drude peak. The sharp peaks below 0.1 eV are attributed to optical phonons. Schematic illustration of the band dispersion for (b) $x = 0$ and (c) $x = 1.2$. The red arrow denotes the optical interband transition at the threshold energy marked with triangles in (a). The horizontal plane indicates the Fermi level E_F. See text for details.

[1] N. P. Armitage, E. J. Mele, and A. Vishwanath, Rev. Mod. Phys. **90**, 015001 (2018).

[2] S. M. Young, S. Zaheer, J. C. Y. Teo, C. L. Kane, E. J. Mele, and A. M. Rappe, Phys. Rev. Lett. **108**, 140405 (2012).

[3] Z. Wang, Y. Sun, X.-Q. Chen, C. Franchini, G. Xu, H. Weng, X. Dai, and Z. Fang, Phys. Rev. B **85**, 195320 (2012).

[4] Z. K. Liu, B. Zhou, Y. Zhang, Z. J. Wang, H. M. Weng, D. Prabhakaran, S.-K. Mo, Z. X. Shen, Z. Fang, X. Dai, Z. Hussain, and Y. L. Chen, Science **343**, 864 (2014).

[5] M. Neupane, S.-Y. Xu, R. Sankar, N. Alidoust, G. Bian, C. Liu, I. Belopolski, T.-R. Chang, H.-T. Jeng, H. Lin, A. Bansil, F. Chou, and M. Z. Hasan, Nat. Commun. **5**, 3786 (2014).

[6] Z. Wang, H. Weng, Q. Wu, X. Dai, and Z. Fang, Phys. Rev. B **88**, 125427 (2013).

[7] M. N. Ali, Q. Gibson, S. Jeon, B. B. Zhou, A. Yazdani, and R. J. Cava, Inorg. Chem. **53**, 4062 (2014).

[8] T. Liang, Q. Gibson, M. N. Ali, M. Liu, R. J. Cava, and N. P. Ong, Nat. Mater. **14**, 280 (2014).

[9] Z. K. Liu, J. Jiang, B. Zhou, Z. J. Wang, Y. Zhang, H. M. Weng, D. Prabhakaran, S.-K. Mo, H. Peng, P. Dudin, T. Kim, M. Hoesch, Z. Fang, X. Dai, Z. X. Shen, D. L. Feng, Z. Hussain, and Y. L. Chen, Nat. Mater. **13**, 677 (2014).

[10] S. Jeon, B. B. Zhou, A. Gyenis, B. E. Feldman, I. Kimchi, A. C. Potter, Q. D. Gibson, R. J. Cava, A. Vishwanath, and A. Yazdani, Nat. Mater. **13**, 851 (2014).

[11] M. Uchida, Y. Nakazawa, S. Nishihaya, K. Akiba, M. Kriener, Y. Kozuka, A. Miyake, Y. Taguchi, M. Tokunaga, N. Nagaosa, Y. Tokura, and M. Kawasaki, Nat. Commun. **8**, 2274 (2017).

[12] Y. Nakazawa, M. Uchida, S. Nishihaya, M. Kriener, Y. Kozuka, Y. Taguchi, and M. Kawasaki, Sci. Rep. **8**, 2244 (2018).

[13] M. Uchida, T. Koretsune, S. Sato, M. Kriener, Y. Nakazawa, S. Nishihaya, Y. Taguchi, R. Arita, and M. Kawasaki, Phys. Rev. B **100**, 245148 (2019).

[14] W. J. Turner, A. S. Fischler, and W. E. Reese, Phys. Rev. **121**, 759 (1961).

[15] C.-Z. Li, L.-X. Wang, H. Liu, J. Wang, Z.-M. Liao, and D.-P. Yu, Nat. Commun. **6**, 10137 (2015).

[16] J. Cao, S. Liang, C. Zhang, Y. Liu, J. Huang, Z. Jin, Z.-G. Chen, Z. Wang, Q. Wang, J. Zhao, S. Li, X. Dai, J. Zou, Z. Xia, L. Li, and F. Xiu, Nat. Commun. **6**, 7779 (2015).

[17] H. Li, H. He, H.-Z. Lu, H. Zhang, H. Liu, R. Ma, Z. Fan, S.-Q. Shen, and J. Wang, Nat. Commun. **7**, 10301 (2016).

[18] Z. Jia, C. Li, X. Li, J. Shi, Z. Liao, D. Yu, and X. Wu, Nat. Commun. **7**, 13013 (2016).

[19] L. Żdanowicz and W. Żdanowicz, Phys. Solid State **6**, 227 (1964).

[20] W. Żdanowicz, K. Lukaszewicz, and W. Trzebiatowski, Bull. Acad. Pol. Sci., Ser. Sci. Chim. **12**, 169 (1964).

[21] W. Żdanowicz and L. Żdanowicz, Annu. Rev. Mater. Sci. **5**, 301 (1975).

[22] H. Lu, X. Zhang, Y. Bian, and S. Jia, Sci. Rep. **7**, 3148 (2017).

[23] S. Nishihaya, M. Uchida, Y. Nakazawa, M. Kriener, Y. Kozuka, Y. Taguchi, and M. Kawasaki, Sci. Adv. **4**, eaar5668 (2018).

[24] S. Nishihaya, M. Uchida, Y. Nakazawa, K. Akiba, M. Kriener, Y. Kozuka, A. Miyake, Y. Taguchi, M. Tokunaga, and M. Kawasaki, Phys. Rev. B **97**, 245103 (2018).

[25] S. Nishihaya, M. Uchida, Y. Nakazawa, R. Kurihara, K. Akiba, M. Kriener, A. Miyake, Y. Taguchi, M. Tokunaga, and M. Kawasaki, Nat. Commun. **10**, 2564 (2019).

[26] S. Thirupathaiah, I. Morozov, Y. Kushnirenko, A. V. Fedorov, E. Haubold, T. K. Kim, G. Shipunov, A. Maksutova, O. Kataeva, S. Aswartham, B. Büchner, and S. V. Borisenko, Phys. Rev. B **98**, 085145 (2018).

[27] H. J. Goldsmid, *Introduction to Thermoelectricity, Springer Series in Materials Science* Vol. 121 (Springer, Berlin, 2009).

[28] C. Zhang, T. Zhou, S. Liang, J. Cao, X. Yuan, Y. Liu, Y. Shen, Q. Wang, J. Zhao, Z. Yang, and F. Xiu, Chin. Phys. B **25**, 017202 (2016).

[29] H. Wang, X. Luo, W. Chen, N. Wang, B. Lei, F. Meng, C. Shang, L. Ma, T. Wu, X. Dai, Z. Wang, and X. Chen, Sci. Bull. **63**, 411 (2018).

[30] T. Zhou, C. Zhang, H. Zhang, F. Xiu, and Z. Yang, Inorg. Chem. Front. **3**, 1637 (2016).

[31] See Supplemental Material at http://link.aps.org/supplemental/10.1103/PhysRevMaterials.5.094201 for additional information on the parameters of the crystal structure determined by single-crystalline x-ray diffraction.

[32] T. Liang (private communication).

[33] G. Landwehr and E. I. Rashba, *Landau Level Spectroscopy, Modern Problems in Condensed Matter Sciences* Vol. 27.2 (North-Holland, Amsterdam, 1991).

[34] D. Maryenko, J. Falson, M. S. Bahramy, I. A. Dmitriev, Y. Kozuka, A. Tsukazaki, and M. Kawasaki, Phys. Rev. Lett. **115**, 197601 (2015).

[35] A. Akrap, M. Hakl, S. Tchoumakov, I. Crassee, J. Kuba, M. O. Goerbig, C. C. Homes, O. Caha, J. Novák, F. Teppe, W. Desrat, S. Koohpayeh, L. Wu, N. P. Armitage, A. Nateprov, E. Arushanov, Q. D. Gibson, R. J. Cava, D. van der Marel, B. A. Piot *et al.* Phys. Rev. Lett. **117**, 136401 (2016).

[36] D. Neubauer, J. P. Carbotte, A. A. Nateprov, A. L'ohle, M. Dressel, and A. V. Pronin, Phys. Rev. B **93**, 121202(R) (2016).

[37] I. Crassee, E. Martino, C. C. Homes, O. Caha, J. Novák, P. Tückmantel, M. Hakl, A. Nateprov, E. Arushanov, Q. D. Gibson, R. J. Cava, S. M. Koohpayeh, K. E. Arpino, T. M. McQueen, M. Orlita, and A. Akrap, Phys. Rev. B. **97**, 125204 (2018).

[38] G. S. Jenkins, C. Lane, B. Barbiellini, A. B. Sushkov, R. L. Carey, F. Liu, J. W. Krizan, S. K. Kushwaha, Q. Gibson, T.-R. Chang, H. T. Jeng, H. Lin, R. J. Cava, A. Bansil, and H. D. Drew, Phys. Rev. B **94**, 085121 (2016).

[39] J. Fujioka, R. Yamada, T. Okawa, and Y. Tokura, Phys. Rev. B **103**, L041109 (2021).

[40] R. Y. Chen, S. J. Zhang, J. A. Schneeloch, C. Zhang, Q. Li, G. D. Gu, and N. L. Wang, Phys. Rev. B **92**, 075107 (2015).

[41] H. Usui and K. Kuroki, J. Appl. Phys. (Melville, NY) **121**, 165101 (2017).